

# Multimodality imaging manifestations of Rosai-Dorfman disease

Acta Radiologica Open  
9(8) 1–15  
© The Foundation Acta  
Radiologica 2020  
Article reuse guidelines:  
sagepub.com/journals-permissions  
DOI: 10.1177/2058460120946719  
journals.sagepub.com/home/arr



Tanvi Vaidya<sup>1</sup> , Abhishek Mahajan<sup>2</sup> and Swapnil Rane<sup>3</sup> 

## Abstract

**Background:** Rosai-Dorfman disease (RDD) is a rare lympho-histiocytic disorder of indeterminate etiology usually presenting with lymph node involvement, and infrequently with extra-nodal manifestations. The diagnosis of this condition is challenging due to the wide spectrum of disease manifestations.

**Purpose:** To elucidate the radiologic features of this disease using multimodality imaging in histopathologically proven cases and to identify characteristic features that would enable its differentiation from its mimics.

**Material and Methods:** We retrospectively evaluated imaging studies of 19 patients with histopathologically confirmed RDD presenting to our institute between January 2004 and March 2016. Imaging modalities included magnetic resonance imaging (MRI), computed tomography, FDG-positron emission tomography (PET) CT, mammography, and ultrasonography.

**Results:** Lymphadenopathy was the most common imaging feature in our study, seen in 11 (57.8%) cases followed by sino-nasal involvement in 7 (36.8%) cases and intracranial masses in 5 (26.3%) cases. Bilateral homogeneously enhancing cervical lymphadenopathy with avidity on FDG-PET scans was the predominant abnormality on imaging. Sino-nasal involvement manifested as homogeneously enhancing soft-tissue masses occupying the paranasal sinuses. Intracranial disease manifested as sellar/suprasellar masses, dural-based lesions along the cerebral hemispheres and choroid plexus enlargement. Unusual disease manifestations included spinal, osseous, and breast lesions.

**Conclusion:** Due to the high likelihood of multifocal involvement, the recognition of RDD at one site necessitates screening of other sites for disease. Homogeneously enhancing, FDG-avid lymphadenopathy and sino-nasal masses in association with hypointense extra-nodal lesions on T2-weighted MRI are imaging features which could aid the diagnosis of RDD and facilitate its differentiation from pathologies that present in a similar manner.

## Keywords

Rosai-Dorfman, lymphadenopathy, paranasal sinuses, computed tomography, magnetic resonance imaging

Received 26 April 2020; accepted 13 July 2020

## Introduction

Sinus histiocytosis with massive lymphadenopathy, formerly described by Rosai and Dorfman as a benign clinicopathologic entity, is characterized by painless cervical lymphadenopathy and histiocytic proliferation (1). Rosai-Dorfman disease (RDD) is exceedingly rare, with a reported prevalence of 1:200,000, more often encountered in children and young adults. Males as well as persons of African ancestry are more frequently affected by the disease (2). Although the precise etiology remains unclear, the disease is believed to be a consequence of an abnormal immune response to certain viral agents, possibly Epstein-Barr virus (EBV), resulting in proliferation of sinusoidal histiocytes,

thus manifesting with lymphadenopathy (1). Though most patients (83%–95%) present with cervical lymphadenopathy, extra-nodal disease involving various sites such as the central nervous system, nasal cavity, orbit, and bones is known to occur (3). Extra-nodal

<sup>1</sup>Department of Radiodiagnosis and Imaging, Ruby Hall Clinic, Pune, India

<sup>2</sup>Department of Radiodiagnosis and Imaging, Tata Memorial Hospital, Mumbai, India

<sup>3</sup>Department of Pathology, Tata Memorial Hospital, Mumbai, India

### Corresponding author:

Tanvi Vaidya Department of Radiodiagnosis and Imaging, Ruby Hall Clinic, Sassoon Road, Pune- 411011, India.  
Email: tanvividya5@gmail.com



involvement has been reported in up to 43% of patients with RDD and is associated with a poorer prognosis than patients with nodal disease alone (3). The diagnosis of RDD on imaging is challenging due to its rarity of occurrence and wide variety of imaging findings (4).

The aim of the present study was to elucidate the gamut of imaging manifestations of RDD using a multimodality approach in order to provide a better understanding of this entity and its varied presentations in clinical practice. To the best of our knowledge, this is one of the largest retrospective single-center studies performed in patients with RDD, with an emphasis on the role of imaging in disease diagnosis.

## Material and Methods

Between January 2004 and March 2016, the electronic medical records at our institution were searched and 19 patients with pathologically proven RDD were selected. Inclusion criteria consisted of a pathologically confirmed diagnosis of RDD with radiologically demonstrable disease and adequate clinical details. We evaluated the available radiologic investigations of the 19 patients, which included magnetic resonance imaging (MRI), computed tomography (CT), fluorodeoxyglucose (FDG)-positron emission

tomography (PET) CT, mammography, and ultrasonography. Moreover, we tried to identify certain imaging features that would enable clinicians and radiologists to differentiate this condition from its mimics. Patient demographics and clinical presentation were also reviewed. Informed consent was obtained for patient imaging. We performed a retrospective review of the patients' medical records and images.

## Results

### Clinical details

Nineteen patients (16 males, 3 females; M:F = 5:1; age range = 13–60 years; mean age at diagnosis = 35 years) were identified with a pathologically proven diagnosis of RDD. Their clinical details are summarized in Table 1. The most common presenting symptom was neck swelling (n = 9, 47%) followed by nasal obstruction (n = 5, 26%).

### Imaging findings

A comprehensive review of the imaging findings and disease pattern is presented in Table 2. Sixteen patients

**Table 1.** Demographics, clinical features, sites of disease, and biopsy sites of patients.

Case no.	Age	Sex	Clinical features	Sites of disease	Biopsy site
1	57	F	Fever, weight loss, blurring of vision in right eye	Intracranial disease, spinal disease, and generalized adenopathy	Cervical lymph node
2	67	M	Nasal obstruction with progressive loss of vision in left eye	Sino-nasal disease, orbital disease	Right nasal mass
3	20	M	Nasal obstruction, neck swelling	Sino-nasal disease, nodal disease, skeletal involvement	Cervical lymph node
4	13	M	Right cheek swelling	Sino-nasal disease, skeletal involvement	Tibial shaft lesion
5	36	M	Nasal obstruction, bilateral knee pain	Sino-nasal disease, skeletal involvement	Nasal cavity mass
6	41	M	Nasal obstruction, right-sided proptosis	Sino-nasal disease, intracranial disease	Maxillary sinus
7	28	M	Neck swelling	Nodal disease	Cervical lymph node
8	32	F	Decreased vision, headache	Intracranial disease, spinal disease	Sellar lesion
9	29	M	Decreased vision in left eye	Intracranial disease	Sellar lesion
10	45	M	Nasal obstruction, neck swelling	Sino-nasal disease, intracranial disease, nodal disease	Nasal mass
11	27	M	Fever, weight loss, neck swelling	Nodal disease, skeletal involvement	Cervical lymph node
12	17	M	Right-sided neck swelling	Nodal disease	Cervical lymph node
13	19	M	Left-sided proptosis	Intracranial disease, orbital, sino-nasal disease	Orbital mass
14	60	M	Abdominal pain, weight loss	Nodal disease, skin involvement, pharyngeal nodal involvement	Retroperitoneal lymph node
15	46	M	Swelling in the neck and groin	Nodal disease, skin involvement	Cervical lymph node
16	52	M	Swelling in the neck	Nodal disease, skin involvement	Cervical lymph node
17	17	M	Swelling in the neck	Nodal disease, skin involvement	Cervical lymph node
18	18	M	Swelling in the neck, weight loss	Nodal disease, pharyngeal disease	Cervical lymph node
19	43	F	Left breast lump	Breast involvement	Left breast mass

**Table 2.** Imaging findings in all patients with Rosai-Dorfman disease.

Case no.	Specific areas of involvement	Imaging features	MRI signal	CT features	FDG-PET features
1	Sellar and suprasellar region, left lacrimal gland, cervico-medullary junction, supra- and infra-diaphragmatic lymphadenopathy	MRI of brain, head, and neck: left lacrimal soft tissue, sellar mass, cervical adenopathy CT: cervical, axillary, mediastinal, retroperitoneal, inguinal, and pelvic nodes	T2W: hypointense lacrimal soft tissue, hypointense cervico-medullary junction and sellar masses T1W: isointense Post-contrast images: homogeneous enhancement	Homogeneous enhancement No bony erosion	–
2	Right nasal cavity, left orbit	MRI PNS: right nasal polyp with left orbital soft tissue	T2W: hypointense T1W: isointense Post-contrast images: homogeneous enhancement	–	–
3	Bilateral nasal cavities, bilateral cervical adenopathy, maxillary alveolus	CT: polypoidal bilateral nasal masses, bilateral cervical lymphadenopathy, lytic lesion in the maxillary alveolus PET CT: FDG-avid masses in bilateral maxillary sinuses, multiple FDG-avid lytic skeletal lesions	–	Homogeneous enhancement No bony erosion	FDG-avid masses in bilateral maxillary sinuses, SUV <sub>max</sub> = 5.5 FDG-avid lytic skeletal lesions, SUV <sub>max</sub> = 6.5
4	Bilateral maxillary sinuses, axial and appendicular skeleton	PET CT: FDG-avid masses in bilateral paranasal sinuses, bilateral maxillary sinuses, FDG-avid lytic skeletal lesions	–	–	FDG-avid masses in bilateral paranasal sinuses, SUV <sub>max</sub> = 11.45; FDG-avid lytic skeletal lesions (SUV <sub>max</sub> = 15.88) noted in the medial condyle of the right femur
5	Bilateral maxillary and ethmoid sinuses, right frontal sinus, bilateral humeri, radius, ulna, tibia, and femur	PET CT: FDG-avid masses in bilateral paranasal sinuses, FDG-avid lytic skeletal lesions	T2W: hypointense T1W: isointense DWI: restricted diffusion Post-contrast images: homogeneous enhancement	Homogeneous enhancement No bony erosion seen	–
6	All paranasal sinuses, right orbit	MRI and CT PNS: soft-tissue masses in all paranasal sinuses, soft tissue in the right orbit	–	–	–
7	Supra- and infra-diaphragmatic lymphadenopathy	PET CT: FDG-avid cervical, axillary, retroperitoneal, external iliac, and inguinal adenopathy	–	–	Bilateral cervical and axillary nodes, max = 2.6 cm, SUV <sub>max</sub> = 14.54 Bilateral external iliac nodes, max = 2.2 cm, SUV <sub>max</sub> = 9.66

(continued)

Table 2. Continued.

Case no.	Specific areas of involvement	Imaging features	MRI signal	CT features	FDG-PET features
8	Sellar, parasellar, and suprasellar region, bilateral temporal convexity, cervico-medullary junction, conus medullaris	MRI of the brain, spine: soft-tissue masses in the sella and parasellar regions, dural-based lesions along bilateral temporal convexities, dural-based spinal lesions CT: no other sites	T2W: hypointense T1W: isointense Post-contrast images: homogeneous enhancement	—	Bilateral inguinal, largest = 6.5 cm, SUV <sub>max</sub> = 18.39 —
9	Sellar and parasellar region	MRI of the brain: sellar lesion compressing the optic chiasma CT: no other sites	T2W: hypointense T1W: isointense Post-contrast images: homogeneous enhancement	—	—
10	All paranasal sinuses, bilateral nasal cavities, dural-based frontal mass, bilateral cervical adenopathy	MRI PNS: sino-nasal masses, dural-based left frontal lesion. PET CT: FDG-avid bilateral cervical lymph nodes, soft-tissue masses in bilateral ethmoid sinuses, right maxillary sinus, and nasal cavity	T2W: hypointense T1W: isointense Post-contrast images: homogeneous enhancement	—	FDG-avid masses in ethmoid sinuses, right maxillary sinus and nasal cavity (SUV <sub>max</sub> = 3.93), no bony erosion; FDG-avid bilateral cervical nodes, max = 2 cm, SUV <sub>max</sub> = 3.49
11	Supra- and infra-diaphragmatic adenopathy, right occipital condyle	PET CT: FDG-avid cervical, axillary, mediastinal, retroperitoneal, mesenteric, pelvic, and inguinal nodes. FDG-avid lytic lesion in the occipital condyle	—	—	FDG-avid lytic lesion in the right occipital condyle, SUV <sub>max</sub> = 25.86; FDG-avid supra- and infra-diaphragmatic adenopathy, max = 3.2 cm, SUV <sub>max</sub> = 30.28
12	Unilateral cervical adenopathy	PET CT: FDG-avid right cervical nodal mass	—	—	FDG-avid right level II cervical nodal mass, max = 5.5 cm, SUV <sub>max</sub> = 12.9
13	Bilateral orbits, choroid plexus, maxillary and ethmoid sinuses	MRI of the brain and orbits: bilateral orbital soft tissue, maxillary and ethmoid soft-tissue masses, choroid plexus nodules CT: no systemic disease	T2W: hypointense T1W: isointense Post-contrast images: homogeneous enhancement	—	—
14	Supra- and infra-diaphragmatic adenopathy, subcutaneous	CT, PET CT: FDG-avid cervical, axillary, mediastinal, and retroperitoneal adenopathy,	—	Homogeneous enhancement	FDG-avid supra- and infra-diaphragmatic adenopathy, max = 2.9 cm,

(continued)

Table 2. Continued.

Case no.	Specific areas of involvement	Imaging features	MRI signal	CT features	FDG-PET features
	nodules, tonsillar and nasopharyngeal involvement	subcutaneous soft-tissue nodule, tonsillar and nasopharyngeal wall thickening	–	–	SUV <sub>max</sub> = 19.30; FDG-avid subcutaneous deposit in right occipital region, SUV <sub>max</sub> = 4.62; bilateral tonsils, SUV <sub>max</sub> = 9.57; FDG-avid nasopharyngeal wall thickening, SUV <sub>max</sub> = 17.09
15	Supra- and infra-diaphragmatic adenopathy, subcutaneous nodules	PET CT: FDG-avid cervical, axillary, retroperitoneal, inguinal adenopathy, subcutaneous nodules	–	–	FDG-avid supra- and infra-diaphragmatic adenopathy, max = 3.7 cm, SUV <sub>max</sub> = 12.5; FDG-avid subcutaneous soft-tissue nodules, SUV <sub>max</sub> = 8.5
16	Supra- and infra-diaphragmatic adenopathy, subcutaneous nodules	PET CT: FDG-avid cervical, axillary, mediastinal, retroperitoneal, mesenteric, and inguinal adenopathy, subcutaneous nodules	–	–	FDG-avid supra- and infra-diaphragmatic adenopathy, max = 4.7 cm, SUV <sub>max</sub> = 13.8; FDG-avid subcutaneous soft-tissue nodules, SUV <sub>max</sub> = 6.3
17	Supra-diaphragmatic adenopathy, subcutaneous nodule	PET CT: FDG-avid cervical and axillary adenopathy, subcutaneous nodule in the right nape of neck	–	–	FDG-avid supra-diaphragmatic adenopathy, max = 3.8 cm, SUV <sub>max</sub> = 6.3; FDG-avid subcutaneous soft-tissue nodules, SUV <sub>max</sub> = 8.85
18	Supra-diaphragmatic adenopathy, nasopharyngeal wall thickening	PET CT: FDG-avid left cervical adenopathy, nasopharyngeal wall thickening	–	–	FDG-avid supra diaphragmatic adenopathy, max = 2.8 cm, SUV <sub>max</sub> = 18.6; FDG-avid nasopharyngeal thickening, SUV <sub>max</sub> = 13
19	Left breast mass	Mammography, USG: left breast mass PET CT: no disease elsewhere	–	–	FDG-PET CT: no systemic disease

CT, computed tomography; DWI, diffusion-weighted imaging; FDG, fluorodeoxyglucose; MRI, magnetic resonance imaging; PET, positron emission tomography; PNS, paranasal sinuses; SUV, standardized uptake value; SUV<sub>max</sub>, maximum SUV; T1W, T1-weighted; T2W, T2-weighted; USG, ultrasonography.

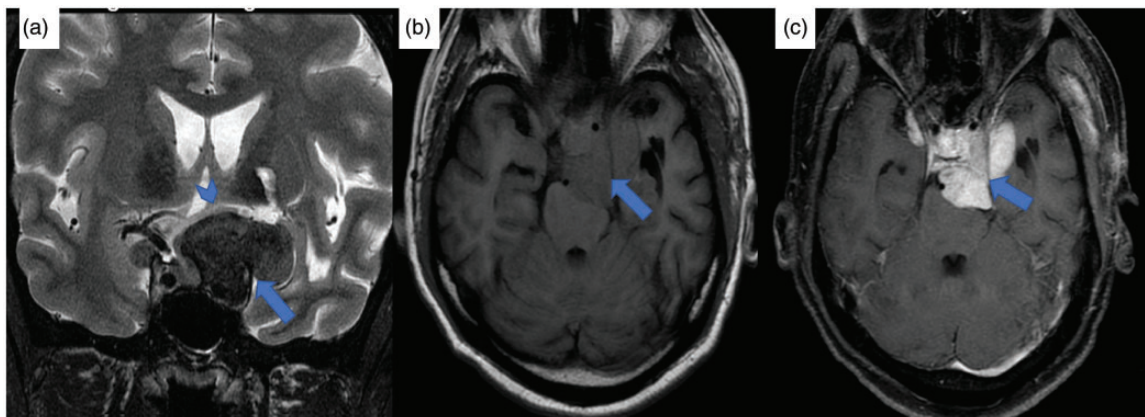


**Fig. 1.** MR images from case 9. (a) Coronal T2-weighted MR image showing a hypointense lesion in the suprasellar region and left cavernous sinus (blue arrow) compressing the optic chiasma (blue arrowhead). (b) On the pre-contrast axial TIW image, the lesion appears isointense (blue arrow) and shows intense homogeneous enhancement on post-contrast TIW images (c, blue arrow). MR, magnetic resonance; TIW, T1-weighted.

had more than one site involved, while three presented with disease at a single site.

**Intra-cranial disease.** Five patients (26.3%) with RDD had intracranial involvement; of which three patients presented with sellar/suprasellar masses, two had dural-based lesions along the cerebral convexity. The dural-based intracranial lesions were located along the temporal and frontal convexities. The sellar/suprasellar masses (Fig. 1) were seen to compress the optic chiasma. No perilesional edema, intralesional calcification, or hemorrhage was seen. There was no evidence of bony erosion or hyperostosis. No enhancing dural tail was seen. One patient presented with choroid plexus involvement, in the form of enlargement and intense contrast enhancement of the choroid plexus in the occipital horns of bilateral lateral ventricles (Fig. 2a and b).

**Orbital disease.** Four patients (21%) presented with orbital involvement (Fig. 3), three with unilateral disease and one with bilateral involvement. One patient had unilateral disease involving the lacrimal gland (Fig. 3c). MRI in this case revealed left lacrimal gland enlargement showing hypointense signal on T2-weighted (T2W) images and intense homogeneous enhancement. Two patients had unilateral intraconal soft-tissue masses, encasing the optic nerve. One patient had bilateral orbital masses in the extraconal compartment.

**Spinal lesions.** There were 2 (10.5%) cases of spinal involvement. Both of these presented with dural-based nodules at the cervico-medullary junction causing cervical cord/brainstem compression (Fig. 4).

One patient also had similar dural-based lesions at the L4 vertebral level and along the conus medullaris. No involvement of the vertebrae or spinal cord was seen.

**Sino-nasal disease.** Seven patients (36.8%) had RDD involving the paranasal sinuses and nasal cavities (Fig. 5a and b). Imaging revealed homogeneously enhancing soft-tissue masses occupying bilateral maxillary, frontal, and ethmoidal sinuses showing uptake of FDG. One patient presented with diffuse para-osseous soft tissue along the bones of the anterior and middle cranial fossa, including the crista galli, body, greater and lesser wings of sphenoid, and pterygoid plates (Fig. 2c and d).

**Osseous lesions.** Four patients (21%) presented with skeletal lesions (Fig. 5c and d). Two of these had multiple sites of disease, involving the axial as well as appendicular skeleton. PET-CT images revealed well-defined, lytic lesions showing FDG avidity. Two patients had solitary bone involvement with lytic lesions in the maxillary alveolus and occipital condyle, respectively (Fig. 5a and b).

**Tonsillar and nasopharyngeal disease.** One patient (5.2%) presented with tonsillar involvement. CT neck revealed bilateral tonsillar enlargement along with diffuse neck lymphadenopathy. FDG-PET revealed hypermetabolism in bilateral tonsils. Two patients (10.5%) presented with FDG-avid nasopharyngeal soft-tissue/wall thickening (Fig. 6a and b).

**Cutaneous disease.** Four patients (21%) had skin involvement in the form of subcutaneous soft-tissue



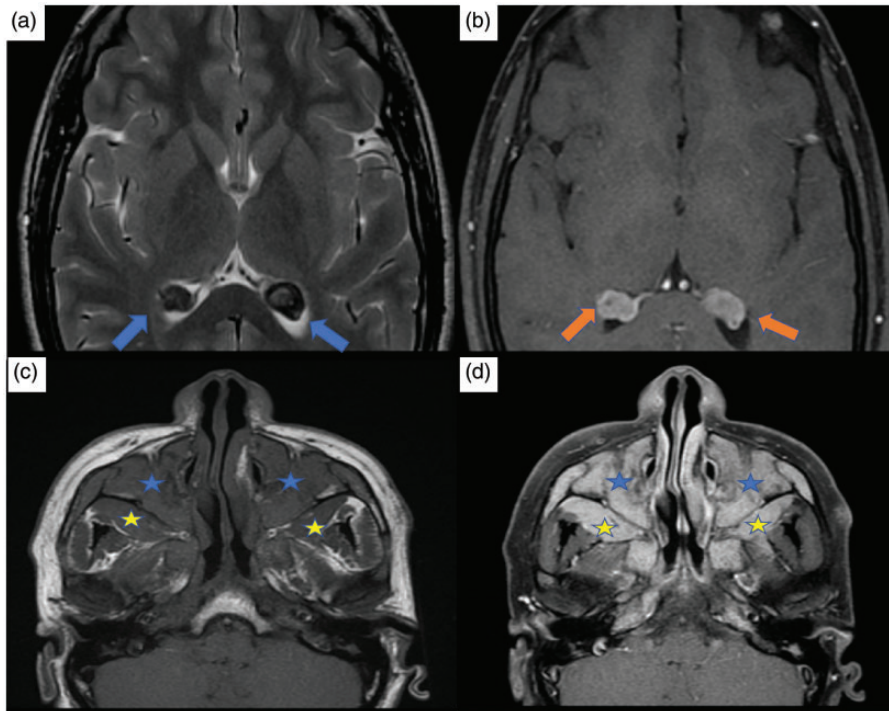


**Fig. 2.** MR images from case 13. (a) Axial T2-weighted MR image showing enlargement of the choroid plexus in bilateral lateral ventricles; these lesions appear hypointense (blue arrows). (b) On the post-contrast axial T1W image, they reveal homogeneous enhancement (orange arrows). (c) Pre-contrast axial T1W images in the same patient show isointense soft-tissue masses in bilateral maxillary sinuses (blue asterisks) and (d) homogeneous post-contrast enhancement (blue asterisks). There is associated para-osseous soft tissue along the maxillary sinuses (c, yellow asterisks) showing homogeneous post-contrast enhancement (d, yellow asterisks). MR, magnetic resonance imaging; T1W, T1-weighted.

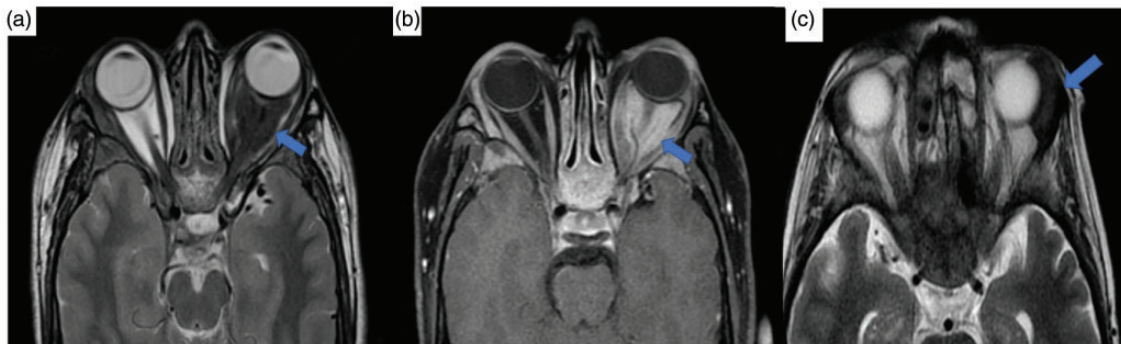


**Fig. 3.** MR images from case 2. (a) Axial T2W MR image showing a markedly hypointense lesion in the left orbit (blue arrow). It involves the intraconal compartment and encases the optic nerve. (b) Homogeneous enhancement on post-contrast T1-weighted images (blue arrow). (c) Axial T2W MR image showing enlargement of the left lacrimal gland, which reveals a hypointense signal (blue arrow). MR, magnetic resonance; T2W, T2-weighted.

nodules in the occipital region, anterior chest, and abdominal wall (Fig. 6c and d); all of these were FDG-avid.

**Lymph nodal disease.** Eleven patients (57.8%) with RDD had lymph node enlargement. All of these presented with supra-hyoid nodal enlargement which included

cervical, retro-pharyngeal, occipital, and intra-parotid nodes: eight bilateral and three unilateral. Six patients additionally had infra-diaphragmatic adenopathy. The nodes showed homogeneous enhancement on CT images. No necrosis was seen. FDG-PET images were available for six patients; all of these revealed avidity on FDG-PET images (Figs. 7a, b, d, e, and 8).

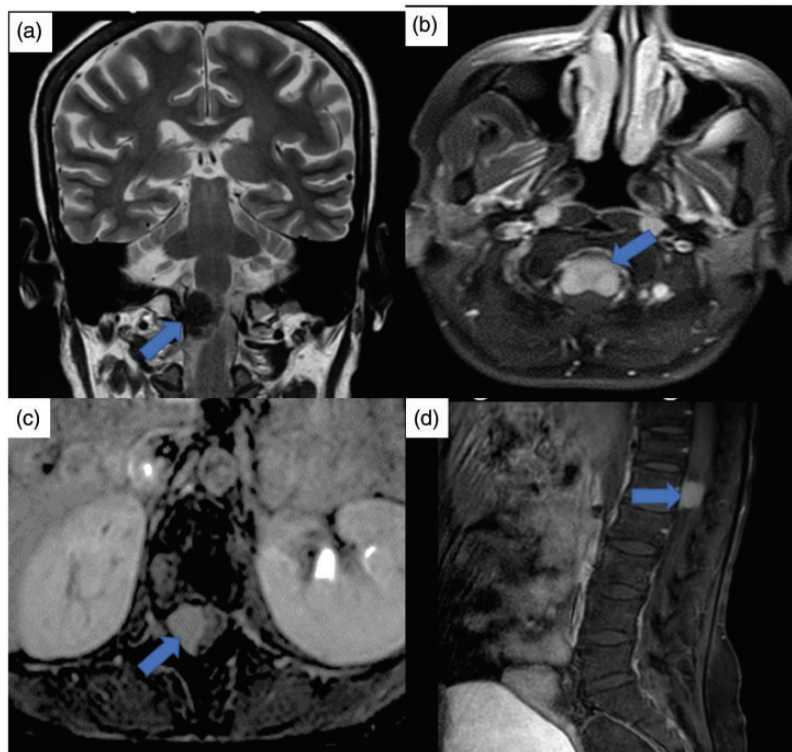


**Fig. 4.** MR images from case I. Coronal T2-weighted MR image showing a dural-based markedly hypointense lesion at the cervico-medullary junction causing cord compression (blue arrow) showing homogeneous post-contrast enhancement (b, blue arrow). (c, d) An enhancing dural-based lesion is also seen at the L4 vertebral level on post-contrast T1-weighted images (blue arrows). MR, magnetic resonance.

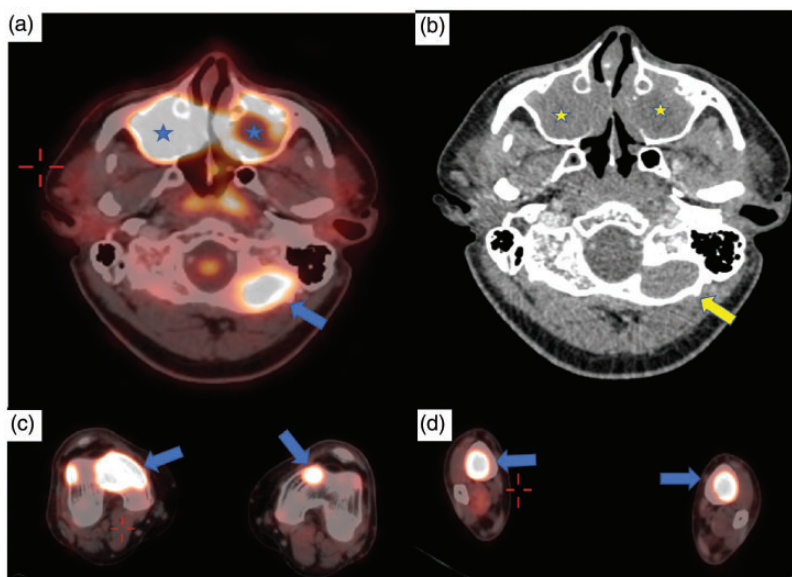


**Fig. 5.** FDG-PET and CT images from case II. (a, b) Bilateral maxillary sinus soft-tissue masses (b, yellow asterisks), showing uptake of FDG (a, blue asterisks). No bone destruction is seen. An FDG avid lesion is seen in the left occipital condyle (a, blue arrow) which appears as a lytic lesion on the CT image (b, yellow arrow). (c, d) FDG-PET images from case 4 show uptake of FDG in bilateral femora (c, blue arrows) and tibiae (d, blue arrows). CT, computed tomography; FDG, fluorodeoxyglucose; PET, positron emission tomography.



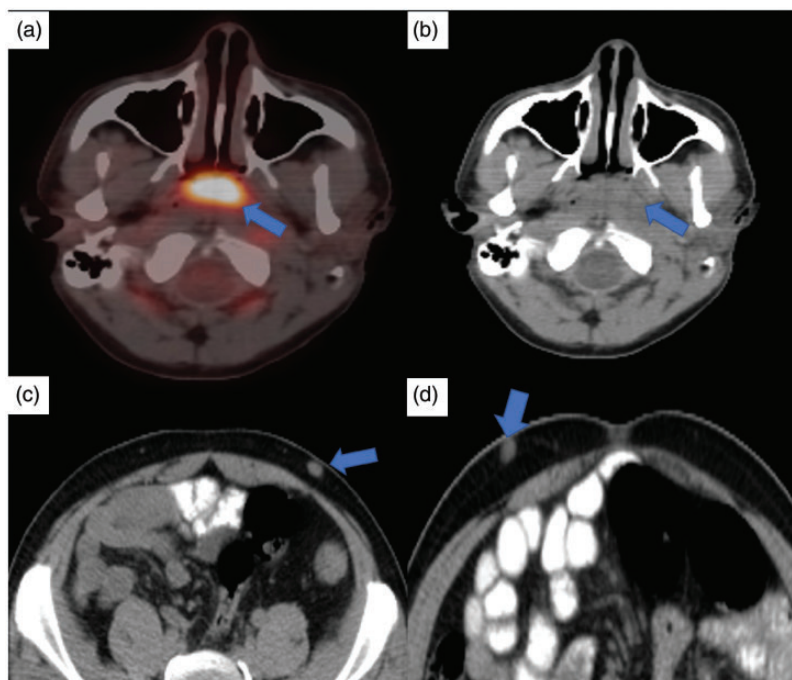


**Fig. 6.** FDG-PET images from case 14. (a, b) A soft-tissue mass is seen occupying the nasopharynx (b, blue arrow), which shows avidity on FDG-PET images (a, blue arrow). (c, d) Non-contrast CT images from case 15 show tiny subcutaneous nodules in the anterior abdominal wall (blue arrows). CT, computed tomography; FDG, fluorodeoxyglucose; PET, positron emission tomography.

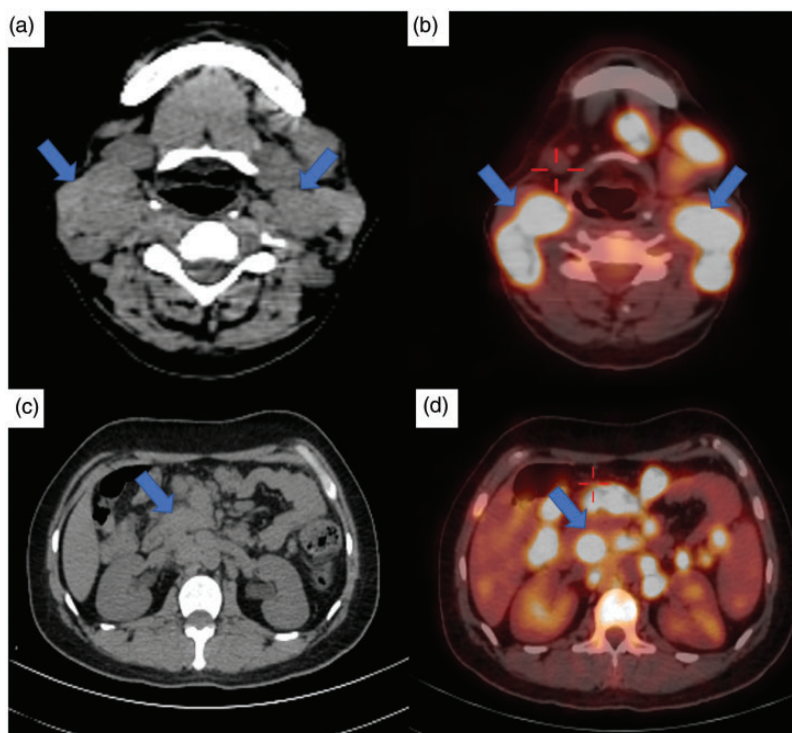


**Fig. 7.** FDG PET and MR images from case 1. (a, b) Enlarged cervical lymph nodes are seen bilaterally on non-contrast-enhanced CT images (a, blue arrows) showing avidity on FDG-PET images (b, blue arrows). Enlarged lymph nodes are also seen in the retroperitoneum on non-contrast-enhanced CT images (c, blue arrows), showing avidity on FDG-PET images (d, blue arrows). CT, computed tomography; FDG, fluorodeoxyglucose; MR, magnetic resonance; PET, positron emission tomography.

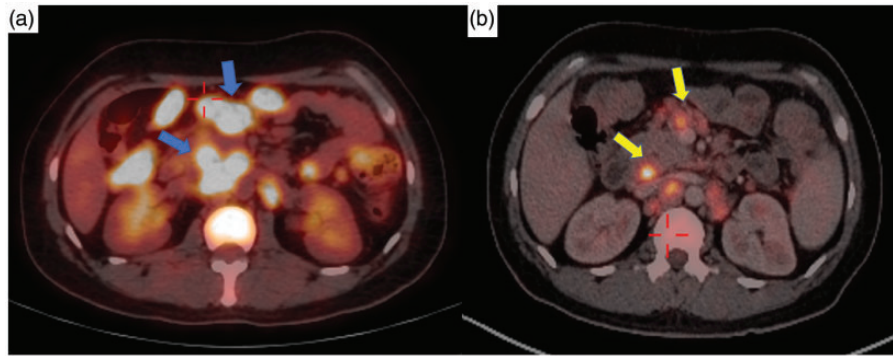


**Fig. 8.** FDG-PET pre- and post-therapy images from case 11. (a, b) FDG-avid enlarged mesenteric and retroperitoneal nodes are seen (a, blue arrows), which reveal a decrease in FDG avidity on post-therapy images (b, blue arrows). FDG, fluorodeoxyglucose; PET, positron emission tomography.

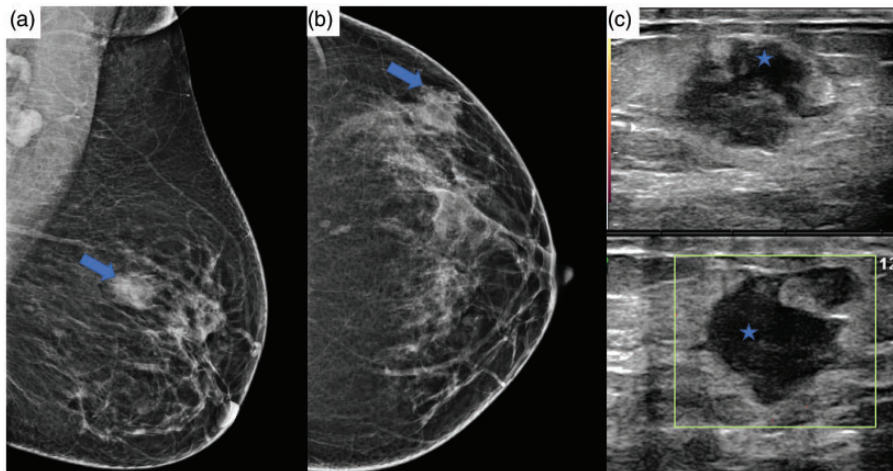


**Fig. 9.** Mammography and ultrasonography images from case 19. (a, b) Left mammogram reveals a high-density spiculated mass in the upper outer quadrant (blue arrows). (c) On ultrasonography correlation, a predominantly hypoechoic lesion with angular margins with no internal vascularity was seen (blue asterisks).

**Breast mass.** One patient (5.2%) presented with a painless swelling in the left breast, gradually increasing in size over a period of two months. Mammography revealed a spiculated mass measuring 3 cm in the upper outer quadrant. On ultrasound correlation, it appeared as a solid, hypoechoic lesion with angular margins at the 3 o'clock position. It was assigned a category of ACR-BIRADS 5 and an excision biopsy was performed, which revealed extra-nodal RDD (Fig. 9). No other sites of disease were seen on FDG-PET study.

### Pathology

Histopathologic examination revealed abundant histiocytes in a sinusoidal pattern, surrounded by ample lymphocytes (Fig. 10). Emperipolesis was observed in 11 (57%) patients.

### Discussion

RDD has a variety of imaging manifestations. We found that majority of our patients had more than one site of involvement, whereas only a few had a single site involved. Thus, the diagnosis of RDD at one site should prompt the treating physician to look for other sites as well (1,3).

The most frequent presentation in the present study was painless cervical lymphadenopathy, which concurs with the original description of the disease (1,3). All cases with lymphadenopathy presented with enlarged cervical lymph nodes, which were bilateral in the majority of cases. This finding is consistent with the original description of the disease (1). Axillary, retroperitoneal, and pelvic/inguinal lymph node enlargement are less frequent compared to cervical adenopathy (1,3–6). Enlarged lymph nodes in RDD reveal homogeneous enhancement on CT images and



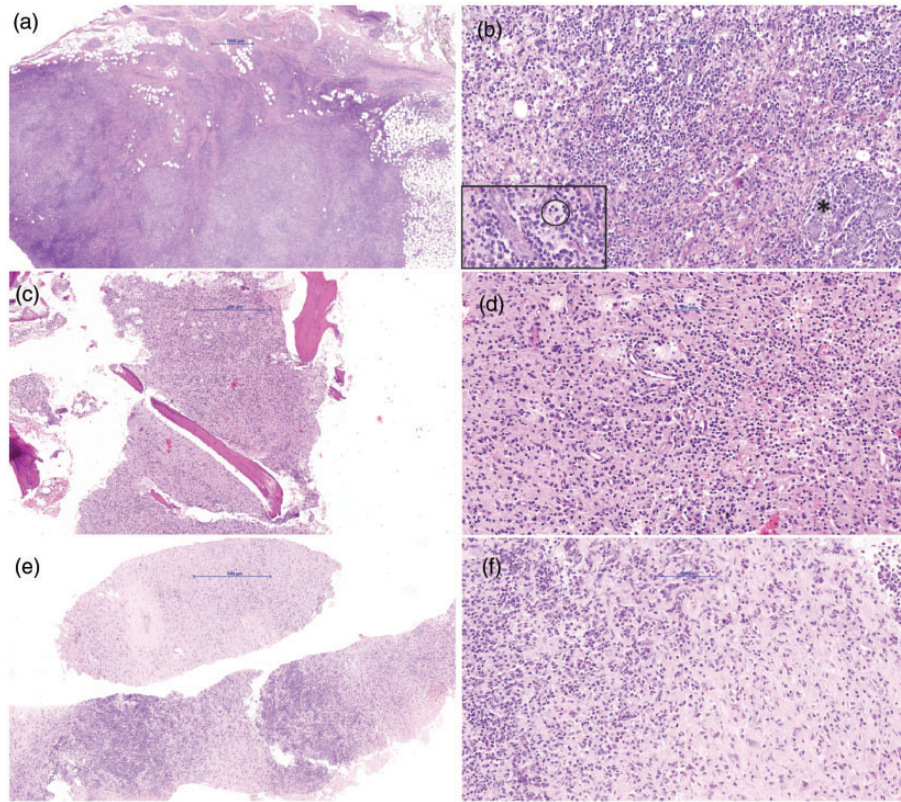


**Fig. 10.** (a) Photomicrograph showing H&E-stained sections of RDD in the breast (50 $\times$  magnification). (b) The native duct-lobular units (\*) are masked by the overwhelming lympho-histiocytic infiltrates (200 $\times$  magnification). Inset shows histiocytes with engulfed lymphocytes and plasma cells without any evidence of destruction (emperipolesis), one instance marked in circle (400 $\times$  magnification). (c) H&E-stained sections of RDD involving bone (50 $\times$  magnification). The bone marrow is replaced by the diffuse histiocytic proliferation which shows (d) emperipolesis (200 $\times$  magnification) and (e) H&E-stained sections of RDD involving the cheek (50 $\times$  magnification). (f) Note the prominent spindling of the histiocytes along with emperipolesis. H&E, hematoxylin and eosin; RDD, Rosai-Dorfman disease.

hypermetabolism on FDG-PET images (3,7), seen in all our cases. Post-therapy FDG-PET images were available in four cases and revealed a decrease in uptake of FDG on post-therapy images, implying that FDG-PET imaging could have a potential role in monitoring response to therapy in RDD (8). Several conditions closely mimic the diagnosis of RDD, primarily those presenting with generalized lymphadenopathy such as lymphoma, Kikuchi disease, and multicentric Castleman's disease (9–11). The differentiation from lymphoma may not be possible on imaging, as both conditions present with multiple nodes that appear discretely enlarged or with soft-tissue masses, showing variable degree of FDG avidity depending on the histological type (9). Kikuchi disease usually presents with unilateral cervical lymphadenopathy and the lymph nodes are reported to be smaller in size compared to those in lymphoma and RDD (10). CT imaging often reveals nodal necrosis and peri-nodal infiltration in Kikuchi disease; these features could aid in differentiating this condition from RDD (10). Certain varieties

of Castleman's disease, such as the plasma cell variety, do not show hyper-enhancing nodes as classically described (11). Instead, they present with generalized lymphadenopathy and may mimic RDD. However, associated imaging features include the presence of hepato-splenomegaly, ascites, and pleural or pericardial effusion, which are not usually seen in RDD (11).

The central nervous system (CNS) is an atypical site of disease, with a reported occurrence in < 5% of cases of RDD (1). In 70% cases of CNS-RDD, the disease is restricted to the brain or spinal cord and is not accompanied by lymphadenopathy (4,12). In intracranial RDD, the usual sites of disease are the cerebral convexities, cavernous sinuses, the suprasellar region, and petro-clival regions (4,12,13). In most cases, a solitary lesion is seen, but multiple intracranial masses have also been reported (14). The sella, suprasellar, and parasellar regions were the most frequent site of CNS disease in the present study. In all cases of intracranial RDD in the present study, the masses were hypointense on T2W images showing homogeneous, intense

post-contrast enhancement, also reported by other investigators (15).

The intra-cranial form of RDD closely mimics neoplasms such as meningiomas, lymphomas, and dural-based metastases, and granulomatous disorders such as sarcoidosis to name a few. We attempted to identify certain imaging features that could aid this differentiation. The signal intensity of meningiomas on T2W images has been reviewed and it has been observed that about 50% of meningiomas appear isointense, 40% appear hyperintense, and only 10% appear hypointense to the brain parenchyma (16). We found that this could serve as a point of differentiation from the dural-based lesions of RDD, as the majority of these lesions appear markedly hypointense on T2W images, an observation noted by us and by other investigators (13,15). The lesions in the present study revealed uniformly low signal intensity on T2W images without calcifications or hemorrhage, confirmed on imaging and pathology specimens. It is believed that the hypointense signal on T2W images could occur secondary to free radical production during phagocytosis; necrotic and fibrotic changes could further contribute to the low signal intensity. Thus, low signal on T2W images favors more of an inflammatory or lymphoproliferative lesion rather than a meningioma (13,17). The absence of bone destruction or hyperostosis and lack of hyper-vascularity on angiography could also aid the differentiation (13).

Hypointensity in meningiomas on T2W images is usually secondary to the presence of calcifications, which reveals blooming on GRE/SW images. This feature has never been reported in RDD; suggesting that the presence of calcifications could prelude the diagnosis of intracranial RDD (18). Primary dural lymphomas may be difficult to distinguish from the dural-based lesions of RDD. The presence of associated features such as plaque-like thickening of the meninges, early invasion of the underlying brain, and bone erosion may serve as clues to the diagnosis (19). Diffusion-weighted imaging may not aid differentiation from lymphoma as restricted diffusion may be encountered in RDD as well due to dense fibrosis within the lesions, limiting movement of water molecules (18).

Dural-based metastases usually appear hyperintense on T2W images, unlike the lesions of RDD which tend to appear hypointense (20). Dural-based lesions of neuro-sarcoidosis serve as close differentials of RDD, owing to the occurrence of a T2W hypointense signal in both conditions. However, the presence of non-contiguous dural enhancement is a feature of dural sarcoidosis which is not seen in RDD (21). Moreover, the posterior fossa is reported to be commonly involved in dural sarcoidosis (22), unlike in RDD.

Orbital involvement in RDD is frequently unilateral with associated lymphadenopathy (23); however, most patients with orbital involvement in the present study did not have associated lymphadenopathy. These patients did in fact have paranasal soft-tissue masses in addition to orbital disease, which could provide a valuable clue to the diagnosis of RDD. Orbital lesions generally appear as infiltrative soft-tissue masses with variable contrast enhancement, involving the lacrimal gland, or intraconal or extraconal compartments (23,24). There is a paucity of available literature on the MRI features of orbital RDD. In our series, it was observed that all orbital lesions had a hypointense signal on T2W images and majority were unilateral. These features have not been reported before and could provide useful clues to the diagnosis. The differential diagnosis of an invasive orbital soft tissue generally includes idiopathic orbital inflammation, lymphoma, granulomatous polyangiitis, sarcoidosis, and IgG4-related disease (23–25). Idiopathic orbital inflammation is more commonly associated with inflammation of the surrounding soft tissues in the form of enhancement of the periorbital soft tissues, infiltration of the pre septal fat, which is infrequent in orbital RDD (26). The presence of bone destruction is more commonly seen in cases of lymphoma and granulomatous polyangiitis and is rare in patients with RDD. Low signal intensity on T2W images is also seen in inflammatory conditions such as idiopathic orbital inflammation, sarcoidosis, and IgG4-related disease, making differentiation difficult, whereas a hyperintense signal could suggest a malignant disease process (27). IgG4-related disease may be difficult to differentiate from RDD due to an overlap of imaging manifestations and sites of involvement. Generalized lymphadenopathy as well as sino-nasal masses, though infrequent, may be encountered in IgG4-related disease on imaging. Nevertheless, certain clues on imaging may aid this differentiation, such as the presence of salivary gland enlargement often in association with bilateral lacrimal involvement, features characteristically seen in IgG4-related disease rather than in RDD (28).

Choroid plexus involvement was an unusual feature encountered by us. Choroid plexus involvement of RDD is an extremely rare occurrence that has been reported only in a few cases (29,30). Even so, RDD should be included as a diagnostic differential in cases with enhancing dural-based masses with associated choroid plexus enlargement showing avid enhancement (30). These features may help to differentiate these lesions from other commonly encountered choroid plexus masses such as papillomas, meningiomas, or granulomatous or inflammatory lesions (30).



Spinal involvement in RDD is uncommon, manifesting as extramedullary dural-based lesions in most cases (4). Most lesions present as homogeneous, iso to hypointense masses on T2W images with or without perilesional edema, a presentation that closely mimics meningiomas (31,32). Distinction from this more commonly occurring imaging abnormality usually requires histologic confirmation. Rarely, the presence of bone hyperostosis may enable the differentiation (32).

The paranasal sinuses constitute the most frequent extra-nodal site of involvement of RDD, manifesting as polypoid masses, with a predilection for the maxillary and ethmoid sinuses (33). The abnormal soft-tissue masses show homogeneous contrast enhancement and increased activity on FDG-PET (34), seen in all our cases. Bone erosion is infrequent in RDD, also noted by us as none of our patients presented with bone erosion (3). This may aid differentiation from sino-nasal malignancies.

Cutaneous involvement is reported to be the second most common extra-nodal site of involvement of RDD, after paranasal sinuses and is reported in 9% of patients with RDD (4). However, purely cutaneous RDD is rare because it usually occurs in conjunction with systemic disease, also observed by us (35,36). In the present study, cutaneous involvement manifested as subcutaneous nodules that were detected incidentally on CT imaging and were FDG-avid. It is essential to identify subcutaneous lesions on imaging, as multifocal soft-tissue disease is a predisposing factor for recurrence, compared to solitary disease (35).

Osseous lesions are seen in 5%–10% of all cases of RDD (4). These usually occur in conjunction with lymphadenopathy or systemic involvement, as seen in all our cases, serving as a clue to the diagnosis. However, isolated skeletal involvement has also been reported, though extremely rare (37). These are often multifocal, usually presenting as lytic intramedullary lesions (38), as seen in the present study. Periosteal reaction and calcifications are typically absent; however, cortical destruction may occur (39,40). FDG avidity was seen on PET imaging; follow-up FDG-PET after therapy revealed decreased uptake at these sites. The top differential diagnoses for such bone lesions are Langerhans cell histiocytosis and lymphoma in children as well as metastases, multiple myeloma, and lymphoma in adults (40).

RDD of the breast is a rare occurrence, with patients classically presenting with painless, palpable, breast masses (41), also seen in the present study (Fig. 9). Mammography may reveal a high-density, lobulated mass with circumscribed or ill-defined margins. On ultrasound, they appear hypoechoic with indistinct or angular margins, showing variable vascularity (42). The presence of a perilesional echogenic halo can be

regarded as a suspicious feature of malignancy (43). In our patient, the mass had spiculated margins on mammography, making it indistinguishable from a primary breast malignancy. The diagnosis was ultimately confirmed on histopathology.

In conclusion, RDD is a rare histiocytic disorder with multisystem involvement manifesting with a broad spectrum of imaging findings. Lymphadenopathy is the most common imaging features and can be isolated, disseminated, or combined with extra-nodal involvement. Extra-nodal disease comprises discrete nodular or mass-like lesions that can affect any part of the body but has a predilection for the head and neck. Considering the likelihood of multifocal involvement, the recognition of RDD at one site necessitates screening for other sites of disease. Awareness of the protean imaging manifestations of RDD could enable clinicians to consider this rare disease as a diagnostic differential in patients with multi-system involvement. Identification of characteristic imaging features can provide a valuable clue to the diagnosis of RDD and aid its differentiation from its mimics. Nevertheless, the definitive diagnosis of RDD should be multidisciplinary and must include a holistic analysis of clinical presentations, imaging manifestations, and histopathologic findings.

#### Declaration of conflicting interests


The author(s) declared no potential conflicts of interest with respect to the research, authorship, and/or publication of this article.

#### Funding

The author(s) received no financial support for the research, authorship, and/or publication of this article.

#### ORCID iDs

Tanvi Vaidya  <https://orcid.org/0000-0002-6290-5628>

Swapnil Rane  <https://orcid.org/0000-0002-5374-3903>

#### References

1. Rosai J, Dorfman RF. Sinus histiocytosis with massive lymphadenopathy. A newly recognized benign clinicopathological entity. *Arch Path* 1969;87:63–70.
2. Abla O, Jacobsen E, Picarsic J, et al. Consensus recommendations for the diagnosis and clinical management of Rosai–Dorfman–Destombes disease. *Blood* 2018;131:2877–2890.
3. La Barge DV 3rd, Salzman KL, Harnsberger HR, et al. Sinus histiocytosis with massive lymphadenopathy (Rosai–Dorfman disease): Imaging manifestations in the head and neck. *AJR Am J Roentgenol* 2008;191:W299–306.

4. Mar WA, Yu JH, Knuttinen MG, et al. Rosai-Dorfman disease: manifestations outside of the head and neck. *AJR Am J Roentgenol* 2017;208:721–732.
5. Mantilla JG, Goldberg-Stein S, Wang Y. Extranodal Rosai-Dorfman disease: clinicopathologic series of 10 patients with radiologic correlation and review of the literature. *Am J Clin Pathol* 2016;145:211–221.
6. Sodhi KS, Suri S, Nijhawan R et al. Rosai-Dorfman disease: unusual cause of diffuse and massive retroperitoneal lymphadenopathy. *Br J Radiol* 2005;78:845–847.
7. McAlister WH, Herman T, Dehner LP. Sinus histiocytosis with massive lymphadenopathy (Rosai-Dorfman disease). *Pediatr Radiol* 1990;20:425–432.
8. Albano D, Bosio G, Bertagna F. 18F-FDG PET/CT follow-up of Rosai-Dorfman disease. *Clin Nucl Med* 2015;40:e420–e422.
9. D'Souza M, Jaimini A, Bansal A et al. FDG-PET/CT in lymphoma. *Indian J Radiol Imaging* 2013;23:354–365.
10. Kwon SY, Kim TK, Kim YS, et al. CT findings in Kikuchi disease: analysis of 96 cases. *AJNR Am J Neuroradiol* 2004;25:1099–1102.
11. Bonekamp D, Horton KM, Hruban RH, et al. Castleman disease: the great mimic. *Radiographics* 2011;31:1793–1807.
12. Huang BY, Zong M, Zong WJ, et al. Intracranial Rosai-Dorfman disease. *J Clin Neurosci* 2016;32:133–136.
13. Zhu H, Qiu LH, Dou YF, et al. Imaging characteristics of Rosai-Dorfman disease in the central nervous system. *Eur J Radiol* 2012;81:1265–1272.
14. Udono H, Fukuyama K, Okamoto H, et al. Rosai-Dorfman disease presenting multiple intracranial lesions with unique findings on magnetic resonance imaging: case report. *J Neurosurg* 1999;91:335–339.
15. Lou X, Chen ZY, Wang FL et al. MR findings of Rosai-Dorfman disease in sellar and suprasellar region. *Eur J Radiol* 2012;81:1231–1237.
16. Ginsberg LE. Radiology of meningiomas. *J Neurooncol* 1996;29:229–238.
17. Sze G, Zimmerman RD. The magnetic resonance imaging of infections and inflammatory diseases. *Radiol Clin North Am* 1988;26:839–859.
18. Hingwala D, Neelima R, Kesavadas C, et al. Advanced MRI in Rosai-Dorfman disease: correlation with histopathology. *J Neuroradiol* 2011;38:113–117.
19. Iwamoto FM, Abrey LE. Primary dural lymphomas: a review. *Neurosurg Focus* 2006;21:E5.
20. Scherer K, Johnston J, Panda M. Dural based mass: malignant or benign. *J Radiol Case Rep* 2009;3:1–12.
21. Shah R, Roberson GH, Curé JK. Correlation of MR imaging findings and clinical manifestations in neurosarcoidosis. *AJNR Am J Neuroradiol* 2009;30:953–961.
22. Ginat DT, Dhillon G, Almast J. Magnetic resonance imaging of neurosarcoidosis. *J Clin Imaging Sci* 2011;1:15.
23. Vemuganti GK, Naik MN, Honavar SG. Rosai dorfman disease of the orbit. *J Hematol Oncol* 2008;1:7.
24. Wang E, Anzai Y, Paulino A, et al. Rosai-Dorfman disease presenting with isolated bilateral orbital masses: report of two cases. *AJNR Am J Neuroradiol* 2001;22:1386–1388.
25. McClellan SF, Aimbinder DJ. Orbital Rosai-Dorfman disease: a literature review. *Orbit* 2013;32:341–346.
26. Pakdaman MN, Sepahdari AR, Elkhamary SM. Orbital inflammatory disease: Pictorial review and differential diagnosis. *World J Radiol* 2014;6:106–115.
27. Shaikh ZA, Bakshi R, Greenberg SJ, et al. Orbital involvement as the initial manifestation of sarcoidosis: magnetic resonance imaging findings. *J Neuroimaging* 2000;10:180–183.
28. Takano K, Yamamoto M, Takahashi H, et al. Recent advances in knowledge regarding the head and neck manifestations of IgG4-related disease. *Auris Nasus Larynx* 2017;44:7–17.
29. Morandi X, Godey B, Riffaud L, et al. Isolated Rosai-Dorfman disease of the fourth ventricle. Case illustration. *J Neurosurg* 2000;92:890.
30. Battal B, Hamcan S, Balyemez U, et al. Choroid plexus involvement in Rosai-Dorfman disease. *Neurol India* 2017;65:222–223.
31. Huang BY, Zhang H, Zong WJ, et al. Rosai-Dorfman disease of rare isolated spinal involvement: report of 4 cases and literature review. *World Neurosurg* 2016;85:367.e11–e16.
32. Xu H, Zhang F, Lu F, et al. Spinal Rosai-Dorfman disease: case report and literature review. *Eur Spine J* 2017;26:117–127.
33. Xu Q, Fu L, Liu C. Multimodality imaging-based evaluation of Rosai-Dorfman disease in the head and neck: A retrospective observational study. *Medicine* 2017;96:e9372.
34. Karunanithi S, Singh H, Sharma P, et al. 18F-FDG PET/CT imaging features of Rosai Dorfman disease: a rare cause of massive generalized lymphadenopathy. *Clin Nucl Med* 2014;39:268–269.
35. Brenn T, Calonje E, Granter SR, et al. Cutaneous Rosai-Dorfman disease is a distinct clinical entity. *Am J Dermatopathol* 2002;24:385–391.
36. Al-Daraji W, Anandan A, Klassen-Fischer M, et al. Soft tissue Rosai Dorfman disease: 29 new lesions in 18 patients, with detection of polyomavirus antigen in 3 abdominal cases. *Ann Diagn Pathol* 2010;14:309–316.
37. Sundaram C, Chandrashekar P, Prasad VB, et al. Multifocal osseous involvement as the sole manifestation of Rosai-Dorfman disease. *Skeletal Radiol* 2005;34:658–664.
38. Foucar E, Rosai J, Dorfman R. Sinus histiocytosis with massive lymphadenopathy (Rosai-Dorfman disease): review of the entity. *Semin Diagn Pathol* 1990;7:19–73.
39. Mosheimer BA, Oppl B, Zandieh S, et al. Bone involvement in Rosai-Dorfman disease (RDD): a case report and systematic literature review. *Curr Rheumatol Rep* 2017;19:29.
40. Gupta P, Babyn P. Sinus histiocytosis with massive lymphadenopathy (Rosai-Dorfman disease): a

- clincoradiological profile of three cases including two with skeletal disease. *Pediatr Radiol* 2008;38:721–728.
41. Tenny SO, McGinness M, Zhang D, et al. Rosai-Dorfman disease presenting as a breast mass and enlarged axillary lymph node mimicking malignancy: a case report and review of the literature. *Breast J* 2011;17:516–520.
  42. Kuzmiak CM, Koomen M, Lininger R, et al. Rosai-Dorfman disease presenting as a suspicious breast mass. *AJR Am J Roentgenol* 2003;180:1740–1742.
  43. Pham CB, Abruzzo LV, Cook E, et al. Rosai-Dorfman disease of the breast. *AJR Am J Roentgenol* 2005; 185:971–972.